

Earth and Space Science



RESEARCH ARTICLE

10.1029/2021EA001914

Key Points:

- The impact of hills on angle and amplitude site errors of lightning location sensors is analyzed by performing 3-D finite-difference time-domain simulations
- Due to propagation losses and limited sensor bandwidth, the angle site errors of first and subsequent return strokes are similar
- The proposed technique can be used for an a-priori site error rating of lightning location systems sensors

Correspondence to:

H. Kohlmann,
h.kohlmann@ove.at

Citation:

Kohlmann, H., Schulz, W., & Rachidi, F. (2021). Evaluation of site errors in LLS magnetic direction finding caused by large hills using the 3D-FDTD technique. *Earth and Space Science*, 8, e2021EA001914. <https://doi.org/10.1029/2021EA001914>

Received 19 JUL 2021
Accepted 8 SEP 2021

© 2021 The Authors. Earth and Space Science published by Wiley Periodicals LLC on behalf of American Geophysical Union.

This is an open access article under the terms of the [Creative Commons Attribution License](#), which permits use, distribution and reproduction in any medium, provided the original work is properly cited.

Evaluation of Site Errors in LLS Magnetic Direction Finding Caused by Large Hills Using the 3D-FDTD Technique

Hannes Kohlmann^{1,2} , Wolfgang Schulz¹ , and Farhad Rachidi² 

¹OVE-ALDIS, Vienna, Austria, ²EPFL, EMC Laboratory, Lausanne, Switzerland

Abstract Angle and amplitude estimation errors in magnetic direction finding, called *site errors*, are important sensor-specific errors in lightning location systems (LLS). They are known to be caused by nearby cables and overhead lines due to induced currents. Due to the reflection and diffraction of electromagnetic waves, hills and mountains are also expected to generate these effects. In this paper, numerical computations applying the finite-difference time-domain (FDTD) method are performed to analyze the impact of hills or mountains on the angle and amplitude estimation of LLS sensors for typical first and subsequent return strokes (RS). The influence of hill size, the distance of sensors to the hill, ground parameters, and sensor bandwidth, are evaluated. The results show that on top of low ridges of only 125 m elevation, up to $\pm 10^\circ$ angle site error and +50% amplitude site error occur. A key finding is that due to field attenuation caused by lossy ground and sensor bandwidth limitations, there is practically no difference in the angle site errors for first and subsequent RS. For two sensors, the average site errors obtained from real sensor measurements are compared to results from 3D-FDTD simulations, modeling the real terrain based on a digital elevation model. The simulation results are in good agreement with the observed, average angle site errors.

1. Introduction

The phenomenon of systematic angle errors of a magnetic direction finding lightning location system (LLS) was addressed in the 1980s, during the early stages in the evolution of LLSs. Hiscox et al. (1984) were among the first authors studying this problem and coining the term “site error.” They found that magnetic direction finding sensors of a LLS network are typically prone to a two-cycle sinusoidal form error when the direction to a return stroke is estimated based on the incident magnetic field (from here on referred to as H-field). This error is caused for instance by buried cables, nearby overhead transmission lines, or objects like large buildings.

In a study concerning the performance evaluation of lightning location systems, Schulz (1997) analyzed site errors in detail by using LLS data. In a subsequent publication about site errors caused by buried cables, Schulz et al. (1998) observed, that also higher order sinusoidal angle site errors, in addition to the two-cycle sinusoidal errors, are observed in evaluations based on LLS data. Later, Schulz and Diendorfer (2002) found that similar to the angle site error, amplitude site errors are expected when the sensors are connected to power supply or communication devices by long buried cables.

The basic principle of these phenomena is that due to the lossy ground, the incident electric field exhibits a horizontal field component along the propagation direction, which in turn causes induced currents along buried cables. This induced current generates an additional magnetic field which couples into the magnetic coil used to detect the incident field and distorts the measured ratio between H_x and H_y components. This results in erroneous estimation of the direction to the return stroke and depends on the angle (azimuth) in the form of a two-cycle sinusoidal function.

Suzuki et al. (2016) have shown that the angle estimation of magnetic direction finders is also influenced by nearby large objects and numerically quantified the effect by means of an FDTD simulation. The subject of this study is to evaluate and verify the existence of another source of angle and amplitude error, which is caused by field reflection and diffraction effects by nearby hills or mountains. The terrain topography at the lightning strike point and the terrain profile along the lightning electromagnetic wave propagation

path has a strong effect on the enhancement or attenuation of the fields that arrive at the sensor site of a lightning location system (LLS) (see e.g., Arzag et al., 2019; Li, Azadifar, Rachidi, Rubinstein, Diendorfer, et al., 2016; Li, Azadifar, Rachidi, Rubinstein, Paoloni, et al., 2016; Li et al., 2014, 2017, 2018, 2019; Hou et al., 2020; Soto et al., 2014; Zhang et al., 2019). In a recent study, Kohlmann and Schulz (2021) computed lightning electromagnetic fields incident at seven LLS sensor sites in Austria, caused by a lightning strike to the Gaisberg Tower, using the 3D-FDTD method. The results revealed that a strike to the mountain top causes a significant field enhancement if special conditions prevail, for example when no tall mountains are present between the strike point and the sensor site. This result was validated by evaluating sensor data of 54 discharges to the Gaisberg Tower.

In order to quantify angle and amplitude site errors caused by reflection and diffraction effects of the terrain at or close to sensor sites, the same full-wave lightning electromagnetic field computation method as in Kohlmann & Schulz (2021) is used in the present study. We performed the 3D-FDTD simulations (see Baba & Rakov, 2016; Taflov & Hagness, 2005; Yee, 1966) utilizing the free and open source software package MEEP (MIT electromagnetic equation propagation—see “MEEP Documentation 2021”; “MEEP Github Repository, 2021”; Oskooi et al. (2010)—whose applicability for lightning electromagnetic field computations was first explored in the study by Kohlmann, 2020). 3D-FDTD simulations were performed in a flat plain and therefore we did not address any diffraction effects originating from the curvature of the earth.

In the present study, two different categories of numerical simulations were performed with respect to the terrain: (a) considering canonical examples with symmetric and asymmetric Gaussian hill shape and (b) considering topographies corresponding to real sensor sites. For these regions, we used a digital elevation model (DEM), which is obtained from shuttle radar topography mission (SRTM, <https://www2.jpl.nasa.gov/srtm/>) data. The novelty of the presented study lies in the fact that the influence of geographic terrain topographies on angle and amplitude site errors of magnetic direction finders of lightning location systems (LLS) has so far not been treated in the literature. The canonic scenarios and their results presented in this article allow us to better understand and evaluate the level of the site errors and their dependence on the height of close-by hills or mountains, the ground conductivity, the sensor bandwidth, and the location of the sensor relative to the terrain. It is also the first time that angle site errors of operative LLS sensors, caused by the surrounding terrain (in contrast to power supply cables), are reconstructed using FDTD simulations. The method can therefore have useful applications in the *a-priori* site error rating of LLS sensors.

This work is structured in the following way: In Section 2 (Methodology), we define the angle- and amplitude site errors and present the means adopted to simulate sensor site errors in the vicinity of hills, ridges, and mountains using the 3D-FDTD approach. In Section 3, we analyze the results and related physical interpretations to gain deeper insight into the phenomena, especially the impact of reflections of the incident lightning electromagnetic fields, caused by close-by hills and ridges, on the site error. Section 4 presents an in-depth discussion on the applicability of the results and insights with respect to real-life problems and improvement in terms of lightning location systems. Section 5 concludes this study by summarizing important findings related to terrain-caused site errors in lightning electromagnetic field sensing.

2. Methodology

2.1. Angle Site Error

The definition of the angle site error is given in Equation 1.

$$\Theta = \alpha + \Theta_{\text{err}} \rightarrow \Theta_{\text{err}} = \Theta - \alpha. \quad (1)$$

The angle Θ (measured angle) is the azimuth angle of the incident magnetic field (H-field) at the sensor site, measured clockwise from the North direction. It is calculated from the ratio of the H_x - and H_y -components, which are the horizontal field components that the magnetic field sensors utilize for peak current and direction estimates. For the direction estimate, the two-parameter arctangent (see (De Dinechin et al., 2015)) can be used

$$\Theta = \text{atan2}(H_x, H_y). \quad (2)$$

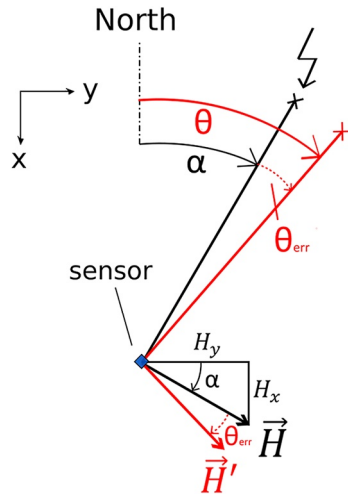


Figure 1. Site error at sensor locations.

The definition of Equation 1 and the H-field components are visualized in Figure 1. The true angle α , is the azimuth between north and the location of the strike point. The angle error Θ_{err} is called *site error*, a deviation added to the true angle α . Reflection and diffraction of the H-field wave front is expected to occur when tall objects, hills or mountains are located close to the sensor site. Since these field components have a different propagation direction compared to the incident plane wave, H_x and H_y components of the H-field vector \vec{H} will be altered (resulting in \vec{H}').

Thus, reflection and diffraction modify the ratio between H_x and H_y in Equation 2 at the moment of the field peak and therefore the estimated angle of incidence Θ contains an estimation error Θ_{err} . The subject of this paper is the examination of this effect caused by hills and mountains with respect to the return stroke type (first and subsequent), various ground parameters and terrain conditions. Throughout this work, the magnetic field vector \vec{H} denotes solely a horizontal field. This choice owes to the fact that the magnetic field sensors normally consist of two perpendicularly aligned magnetic loop antennas which record the H_x - and H_y -components, the vertical component H_z not being measured. Also, the propagation direction vector \vec{k} , which is estimated (technically, the vector \vec{k}

can only be estimated by an LLS sensor after taking the polarity of the incident vertical E-field E_z into consideration, which indicates whether the lightning discharge was positive or negative) from \vec{H} assuming plane wave conditions, considers only horizontal and no vertical components.

2.2. Amplitude Site Error

In addition to a rotation of the H-field vector from \vec{H} to \vec{H}' , as shown in Figure 1, it is expected that the reflections and diffraction caused by elevated terrain will also lead to local enhancement or attenuation of the magnitude of the rotated H-field vector \vec{H}' compared with the unaltered vector \vec{H} . We therefore define a magnitude error

$$\eta_A = \frac{|\vec{H}'| - |\vec{H}|}{|\vec{H}|}, \quad (3)$$

$$|\vec{H}| = \sqrt{H_x^2 + H_y^2},$$

which compares the magnitude $|\vec{H}'|$ obtained assuming a flat ground with $|\vec{H}'|$ obtained from simulations taking into account the terrain profile. An attenuation will lead to values of $\eta_A < 0$ while an enhancement to $\eta_A > 0$.

2.3. Return Stroke and Lightning Current

Two types of return stroke (RS) are simulated, a first RS and a typical subsequent RS. We used the same channel-base currents as in Soto et al. (2014) or Rachidi et al. (2001), where the first RS has its peak amplitude at $8.5 \mu\text{s}$ and the subsequent RS at $0.85 \mu\text{s}$. Therefore, the subsequent RS has a shorter rise time and a higher maximum current derivative compared to the first RS. The channel is represented by the modified transmission line model with exponential current decay (MTLE) model (see Nucci et al., 1988 and Rachidi et al., 2001), with a return stroke wavefront speed of $v_{\text{RS}} = 1.5 \cdot 10^8 \text{ m/s}$ and an exponential spatial current decay constant of $\lambda = 2 \text{ km}$. The return stroke current model was implemented in MEEP using a phased-current-source array (see Baba & Rakov, 2016).

2.4. MEEP Simulation Parameters

The following parameters were used for the simulation. The 3D-FDTD spatial resolution was specified as $\Delta x = \Delta y = \Delta z = 25 \text{ m}$ (one-twentieth of the shortest wavelength associated with the subsequent return

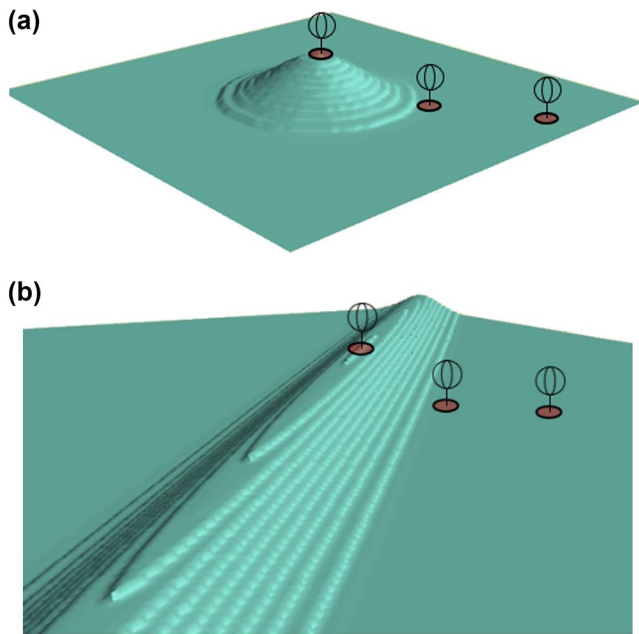


Figure 2. Terrain objects (250 m elevation) initialized in MIT electromagnetic equation propagation. Sensor locations considered in this study are schematically indicated.

stroke) with a Courant factor S of 0.57, leading to a time step $\Delta t = 48$ ns. Those parameters were chosen to get a reasonable computation time while retaining the characteristics of the return stroke waveform and preventing numerical dispersion. The simulation domain was set as a corridor with a width of 10 km and a length of 50 km. The height of the corridor was set to only 4 km in order to save computation time. The domain is terminated by perfectly matched layers (PML) of 0.5 km thickness on each side of the corridor. Depending on the elevation of the strike point in the real terrain scenario, the return stroke channel lengths were between 3 and 4 km. For the adopted return stroke velocity of $v_{RS} = 1.5 \times 10^8$ m/s and a channel length of 3 km, the return stroke current pulse reaches the PML after approximately $20 \mu\text{s}$. The expected field reaches its peak at the observation point in 40 km distance not later than $10 \mu\text{s}$ and the artificial termination has no impact on the field peaks and the results when determining the angle site errors.

Due to unwanted reflections of obliquely incident fields at the PML interface, (Kohlmann & Schulz, 2021), observation points closer to the simulation cell boundaries will exhibit artificial site errors. However, a reference simulation to determine the fields over flat ground was performed, where the artificial site errors caused by the cell boundaries is the same as in the terrain simulation. Subtracting the H-field vectors obtained from the reference simulation considering flat ground from the terrain simulation results at corresponding observation points allows to determine the angle site errors as well as to compensate for the effect of the spurious wave reflections close to the cell boundaries.

2.5. Simulated Objects

The considered geometries used to simulate site errors for canonical cases are illustrated in Figure 2: In one scenario the terrain object influencing the incident H-field at the sensors is assumed to be a symmetric Gaussian hill (Figure 2a) of 1.5 km diameter at the base of the hill; in the second scenario, an asymmetric Gaussian hill with 1.5 km width but 60 km length (Figure 2b) is considered to represent a ridge-like terrain structure. A top-down view of these hills is depicted in the center of the graphic in Figure 3. In this schematic, the x - and y -coordinates are indicated, the distance from the hill center to the strike point d is set to 40 km. The site errors are simulated for different elevations h of the hills (125, 250, and 500 m). The sensor locations, which are indicated in Figures 2 and 3 (blue diamonds), represent the observation points at horizontal distances (denoted with s) of 0, 0.75, and 1.5 km from the origin O of Figure 3.

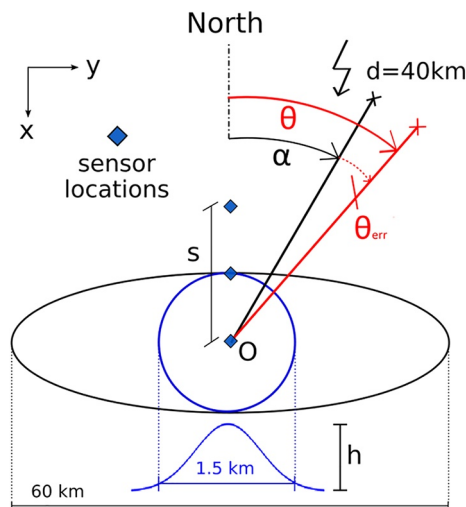


Figure 3. Site error at sensor locations (not in scale). The blue line corresponds to the symmetric Gaussian hill (Figure 2a) and the black line to the asymmetric Gaussian hill (Figure 2b).

The site errors depend on the true angle α of the stroke location when the terrain topography (here the geometrical objects) and the sensor locations are fixed. To obtain the site errors along the azimuth for an asymmetric hill (see Figure 3, black ellipse), the strike point is rotated around the origin O (Figure 3) by increments of $\Delta\alpha = 5^\circ$ relative to the object in each simulation, while keeping the hill center at the same distance to the origin. Due to partial symmetry, simulating 0° – 180° suffices to determine the angle site error for a full turn, thus only 36 iterations instead of 72 are necessary. In the symmetric Gaussian hill scenario (Figure 3, blue circle), all site errors along the azimuth can be evaluated in one single simulation with good accuracy by rotating the sensor around the center of the hill.

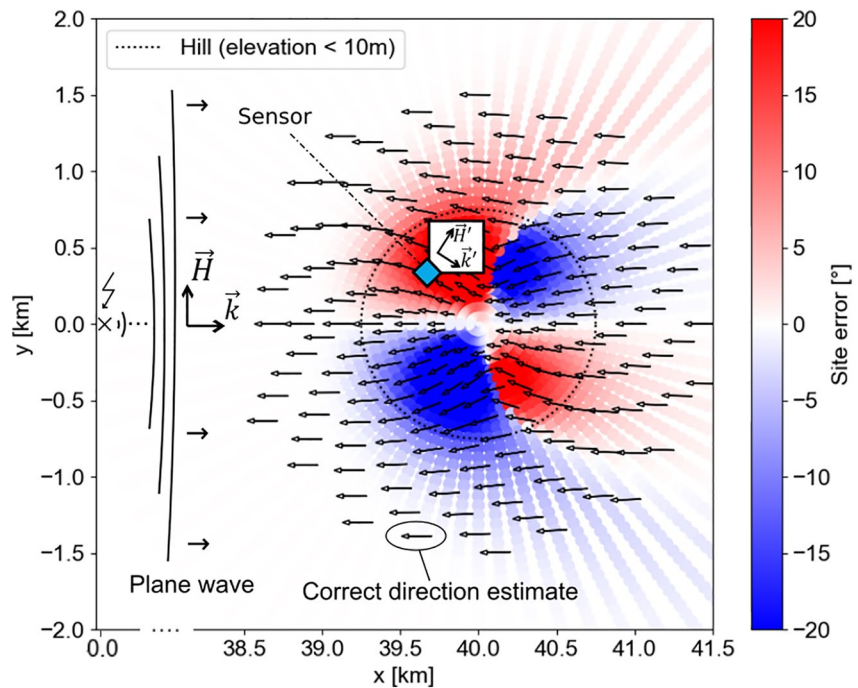


Figure 4. Angle site error (in $^{\circ}$) caused by a symmetric hill ($h = 500\text{m}$) for a subsequent return stroke striking the origin of the coordinate system. The ground conductivity is 1 mS/m . The set of arrows point into the estimated direction of incidence. Their rotation with respect to the x -axis corresponds to the site error in degrees (different arrow lengths only serve for better visualization). The sensor location is shown using the blue diamond. The resulting angle site error is indicated using color code. The radial beams that become apparent in the colored site error pattern in the eastern region, beyond the dash-dotted line, are artificial and caused by the polar coordinate sampling, with constant angle steps of $\Delta\alpha = 5^{\circ}$. The white space between those beams must not be interpreted as interference patterns, but missing sample points instead.

2.6. Processing and Evaluation

The incident angle estimated by the LLS sensor and therefore also the site errors are determined at the time at which the field reaches its maximum, that is, $|\vec{H}| = \sqrt{H_x^2 + H_y^2}$ (see Equation 3) attains the highest amplitude. This represents the behavior of LLS sensors which sample two perpendicular H-field components of the incident wave, using two crossed magnetic loop antennas. The ratio between H_x and H_y used to estimate the angle of incidence is also determined at the time instant when the squared sum of the two components is maximum. To take into account the LLS sensors bandwidth, a 400 kHz second-order Bessel filter has been applied to all field waveforms before evaluating site errors throughout the work, unless otherwise indicated.

3. Results

In this section, the results of the computed angle and magnitude site errors are presented for three different distances of the sensor site from the origin O (see Figure 3) as a function of the true azimuth angle α : $s = 0\text{ km}$ (top of the hill), $s = 0.75\text{ km}$ (foot of the hill) and $s = 1.5\text{ km}$. Further, the influence of the ground conductivity on the site errors is investigated.

3.1. Angle Site Error

First, the qualitative nature of angle site errors and the techniques that were employed for their determination are explained. The illustration in Figure 4 presents the top view of a symmetric hill of elevation $h = 500\text{ m}$ and a diameter of 1.5 km . The dotted-line circle denotes the hill's perimeter where the elevation has declined to less than 10 m . A lightning flash strikes at point $(0, 0)\text{ km}$ at the middle of the left side y -axis and radiates an electromagnetic wave, which develops approximately into a plane wave (labeled in Figure 4)

with increasing distance. It approaches the hill from the left. The local horizontal propagation direction \vec{k} is indicated by the arrows pointing rightwards. When the wave front reaches the elevated terrain, parts of the wave are reflected and diffracted. These reflected and diffracted fields, with different orientations compared to \vec{k} , are superimposed to the H-field vector \vec{H} of the main incident plane wave. A sensor on or close to the hill (see the blue diamond in Figure 4) will therefore register a rotated field vector \vec{H}' . This suggests a wrong propagation direction \vec{k}' instead of the true propagation direction \vec{k} . The application of Equation 2 will yield an estimated direction of incidence that has an angle site error indicated for all grid points by the color scheme. Deep red is larger than $+20^\circ$ and deep blue is smaller than -20° . For better visualization of the error, a set of arrows oriented to the left indicate the estimated direction Θ (the length of the arrows is insignificant and only serves the purpose of better visualization). If no site error prevails (white region), the arrows represent a correct direction estimate pointing accurately toward the lightning strike point (arrows parallel to the x-axis). At the colored areas around the hill, the arrows are rotated according to the angle site error Θ_{err} (see Equation 1), that is, clockwise if positive (red) or counter-clockwise for negative (blue) Θ_{err} . In our example in Figure 4, both the lightning strike point and the sensor (Figure 4, blue diamond) lie in the west of the hill ($\alpha = 270^\circ$). Given that the sensor has a small spatial offset of only 250 m in the y-direction compared to a distance of 40 km, the strike point lies approximately at $\alpha = 270^\circ$ relative to the sensor. At the marked point, the sensor would measure the rotated field \vec{H}' , as shown in the inset in Figure 4, and estimate an angle with a site error of approximately $\Theta_{\text{err}} = +20^\circ$. Applying Equation 1, the estimated angle of incidence Θ is, therefore, $\Theta = \alpha + \Theta_{\text{err}} = 270^\circ + 20^\circ = 290^\circ$ (west-northwest).

Figure 4 shows the site error for *only one discrete angle* of field incidence, that is, where $\alpha = 270^\circ$. As stated in Sections 2–2.5, to get the 360° site error behavior, the simulation has to be repeated for 72 increments of $\Delta\alpha = 5^\circ$ to rotate the strike point around the sensor. This is the procedure in the non-symmetric scenario where the site errors and arrow orientations change significantly at each increment $\Delta\alpha$. However, in the fully symmetric case, all information can be gained and the site error computed with only one simulation. Even though the knowledge of the strike point would be sufficient to estimate the angle site error along the azimuth, a reference \vec{H} field evaluated above a flat ground in a separate simulation was considered. In addition to determining the angle site error accurately, this method has the advantage that spurious effects at the cell boundary can be compensated for. Site errors caused by the ridge (see Figure 2b) were simulated by rotating the object and the sensor locations counter-clockwise with $\Delta\alpha$ to keep the corridors equally small in size.

We now present the angle site errors over the full range of 0° – 360° . The graphs originate at $\alpha = 0^\circ$ (lightning discharge in the north) and correspond to the scenario shown in Figure 3, where the asymmetric hill is perpendicular to the north. We investigate the effect of different hill elevations h on the angle site errors for different sensor locations. The plots are presented side-by-side for both the ridge (asymmetric hill) and symmetric hill in Figures 5a and 5b, respectively.

We first analyze the results of the **asymmetric** case (ridge) in Figure 5a. As one would expect, an increase in elevation correlates with an increase of the maximum site errors. For a sensor located on the top of the ridge ($s = 0$ km, top graph in Figure 5a), the site error is a double-cycle sinusoidal function and sign-reversed compared to sensors that are located at the foot of the ridge ($s = 0.75$ km, Figure 5a center) and further away ($s = 1.5$ km, Figure 5a bottom). While on the top of the ridge the double-cycle sinusoidal site error appears to decrease quasi-linearly with decreasing elevation h , a much stronger reduction of the site error with decreasing elevation is noticeable at the foot of the ridge and further away. However, for higher elevations ($h = 500$ m), the maximum occurring site error at $s = 0.75$ km and $\alpha = 300^\circ$ is even larger compared to the maxima at the top of the ridge ($s = 0$ km), as this location is specifically prone to immediate reflections along a broad and steep surface. In turn, doubling up the distance from $s = 0.75$ km to $s = 1.5$ km leads to a significant reduction of the maximum site error to less than one-fifth, which holds true for all elevations (compare Figure 5a center with bottom graph). I.e., for $h = 500$ m this means a reduction of the maximum site error from 20° to 3° . It is worth highlighting that at the highest point of the ridge even smaller elevations (compare $h = 125$ m) exhibit considerable site errors of up to $\pm 10^\circ$.

For the **symmetric** hill, Figure 5b, similar conclusions can be drawn. The only significant difference is that on the top of the hill the site error is constant due to symmetry and negligibly small. However, there the sensitivity of the site error to small offsets from the center is high, as can be understood from Figure 4. In

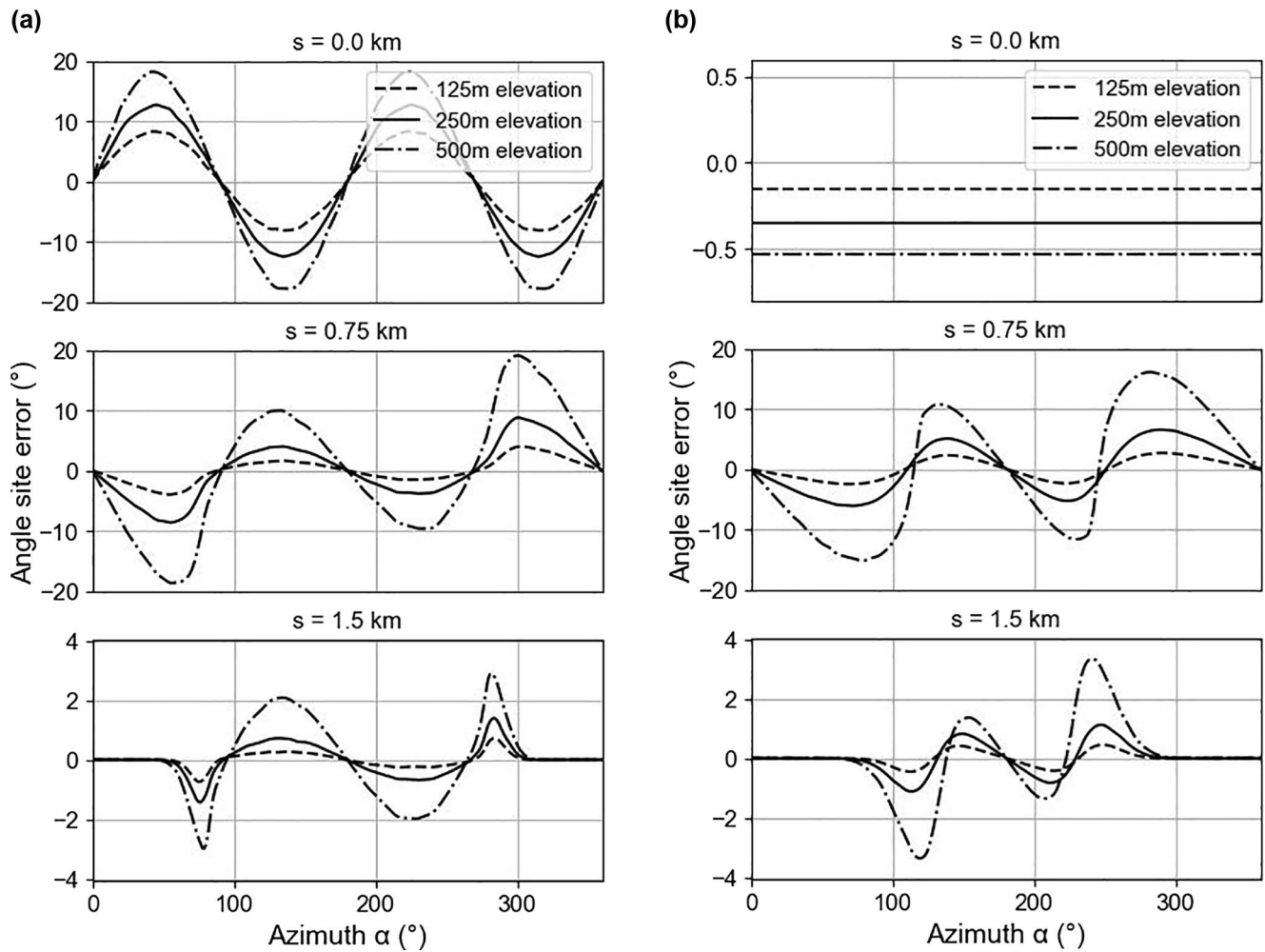


Figure 5. Angle site error for a subsequent RS, (a) Asymmetric versus (b) Symmetric hill; $\sigma = 1$ mS/m.

case of wrong positioning or a slight asymmetry, large angle site errors have to be expected. At the foot of the symmetric hill ($s = 0.75$ km, Figure 5b) slightly smaller site errors are observed compared to the ridge due to the absence of large surfaces acting as reflection planes. With respect to these results, it should be considered to install magnetic field sensors at locations as far away from hills or ridges as possible.

3.1.1. Reflections and Diffraction

At this point, it is important to distinguish between, and interpret, the observed site errors along the azimuth α as components dominated by *reflections*, where the sensor is located between the hill and the lightning strike point (with no obstacle in between), and *diffraction*, where the sensor is located “in the shadow” of the hill where reflections cannot occur. The most significant impact of the transition from *reflection* to *diffraction* regions is the change in the sign of the angle site error. This transition can be seen in Figure 4 for the symmetric hill, where the color changes abruptly from blue to red and the arrows rotate accordingly in the north-northeast and south-southeast above the hill center. In the case of the asymmetric hill, this transition is observed close to 90° , where the ridge is “in line” with the lightning strike point. This is expected as a consequence of the prevailing geometric symmetry where reflections cannot appear. We observe for both the ridge and the symmetric hill a very steep transition of the site error at this break point. Another observation, common to both scenarios, is that the more distant from the hill or ridge is the sensor, the narrower is the range of the azimuth angles over which a significant site error occurs. This can be explained by appropriate propagation time differences between the main incident field and the reflected waves, which have to prevail (see in-depth discussion in Section 4). Specifically, the non-zero site error range is narrowed

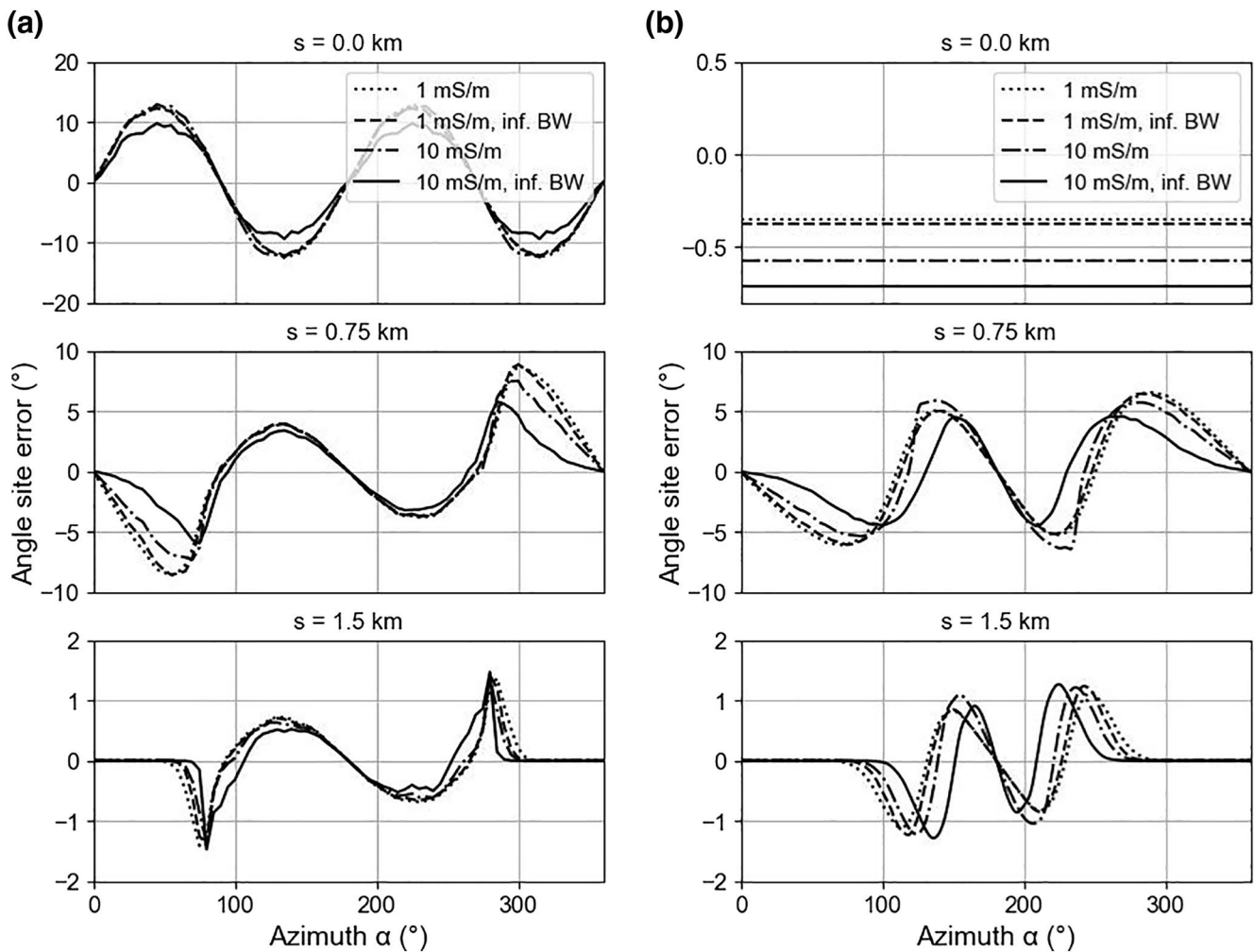


Figure 6. Conductivity dependence of the angle site error for a subsequent return stroke, (a) Asymmetric versus (b) Symmetric hill with $h = 250$ m. The legend “inf BW” indicates sensors with infinite bandwidth.

down to a range between $\alpha = 60^\circ$ and $\alpha = 300^\circ$ for the ridge and $\alpha = 80^\circ$ to $\alpha = 280^\circ$ for the symmetric hill, at $s = 1.5$ km (Figure 5, bottom graphs). For larger distances s , the reflection component below $\alpha = 90^\circ$ will degenerate and eventually disappear in case of the ridge. Only a diffraction component will remain between $\alpha = 90^\circ$ and $\alpha = 180^\circ$.

At the foot of the ridge ($s = 0.75$ km, Figure 5a center), the maximum site error caused by the reflection components is twice as high ($\Theta_{\text{err}} = \pm 20^\circ$ vs. $\Theta_{\text{err}} = \pm 10^\circ$ for elevation $h = 500$ m) at about $\alpha = 60^\circ$ compared to the site error caused by diffraction components at $\alpha = 130^\circ$ and 230° . The reflections originating from the broad surface of the ridge, which is oriented toward the lightning event, have a high impact on the angle site error. These reflections are expected, and observed, between $\alpha = 0^\circ$ and 90° and $\alpha = 270^\circ$ – 360° (Figure 5a center and bottom). For larger distances of the sensor to the ridge, reflections from only a narrow azimuth range have an impact on the angle site errors (see the positive/negative notches at about $\alpha = 80^\circ$ and $\alpha = 280^\circ$ in Figure 5a, bottom). Also, the site errors caused by reflection components are reduced with decreasing elevation of the ridge.

Next, we investigate the dependence of the angle site error for a subsequent RS considering different values for the ground conductivity ($\sigma = 1$ and 10 mS/m). The hill elevation here is $h = 250$ m. The results are shown in Figure 6. Here, the effect of the ideal sensor, that has infinite bandwidth is plotted separately (Figure 6, “inf. BW”). The unfiltered case (Figure 6, solid and dashed) can be thought of as a site error from a sensor with a much higher bandwidth. For such a sensor short rise times would be retained which has

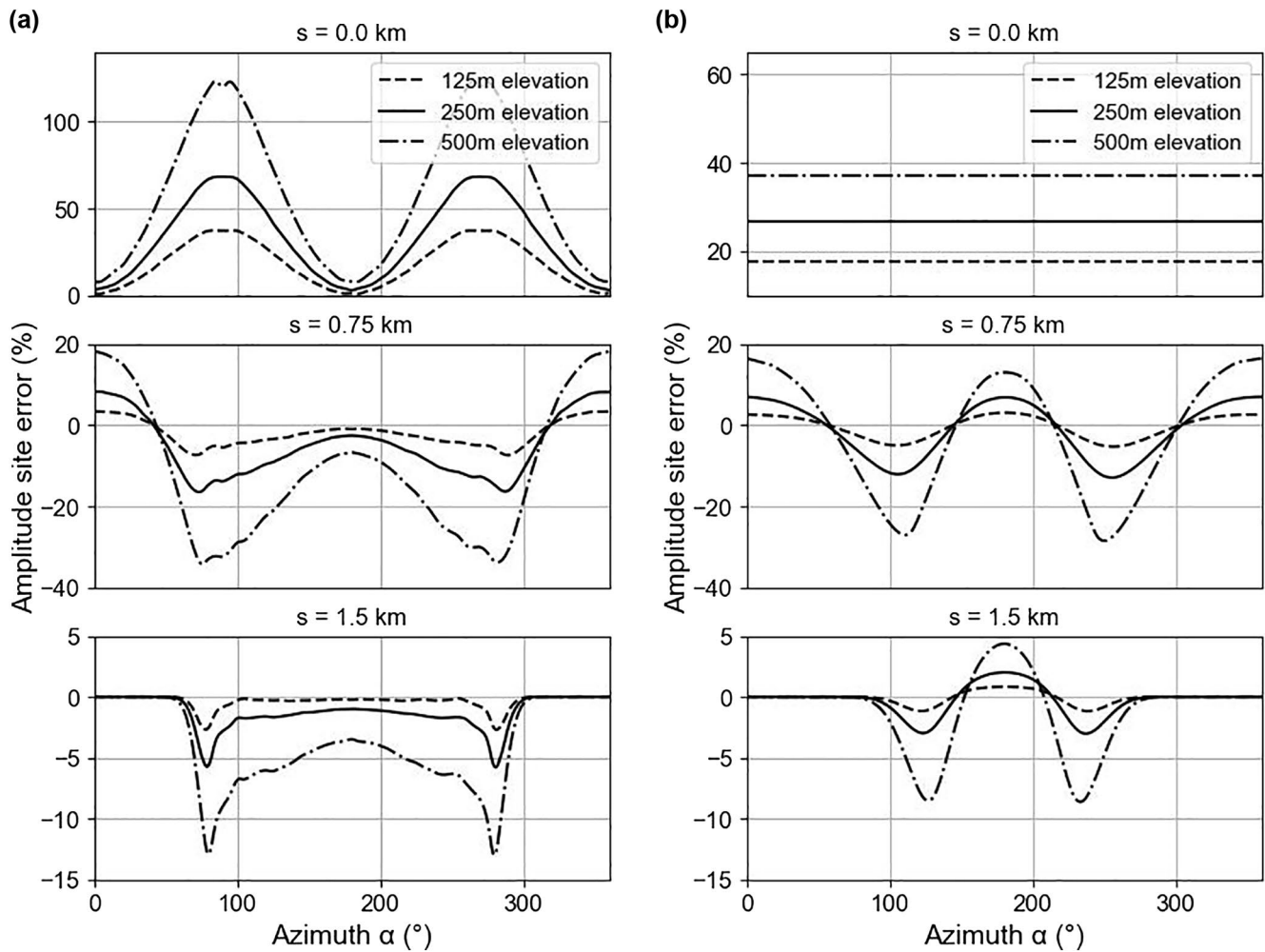


Figure 7. Elevation dependence of the amplitude site error (subsequent return stroke), $\sigma = 1$ mS/m, (a) Asymmetric versus (b) Symmetric hill.

an important consequence regarding the site error behavior. The results support the physical and technical explanation of reflections in the previous paragraphs well and allow for further interpretation regarding the connection between the rise time of the main incident field, the propagation delay of reflected waves, and the expected site errors.

The most obvious effect is that good ground conductivity (10 mS/m) retains short rise times due to less filtering of high frequencies along the propagation path. Therefore, the field peak, which is dominantly determined by the main incident wave, is sampled earlier with a sensor of (infinitely) high bandwidth (Figure 6, solid). As a consequence, the time difference between the main field peak and the arrival time of the reflected waves is increased and the site errors are reduced (see Section 4). The resulting shift of the site errors toward larger angles α is clearly visible in the center and bottom graphs of Figure 6 for both the asymmetric and symmetric hill scenarios. Especially for a sensor located at a distance of $s = 1.5$ km from the ridge (Figure 6a, bottom, compare also Figure 5a, bottom), the narrow notch is shifted toward $\alpha = 90^\circ$.

As the 400 kHz filter is added, the recorded field peak will occur at a later time, reducing the time difference between the main field peak and reflected fields. Thus, the reflected fields have an impact at smaller azimuths α , and the maximum site error increases. This is the case in both geometric scenarios where the sensor is located at $s = 0.75$ km and $s = 1.5$ km. The only exception is the symmetric hill, where the filter has a slightly attenuating effect on the site error for larger sensor distances (Figure 6b, bottom). The diffraction parts of the site error are less affected by different ground conductivities and thus appear similar for all scenarios. On the top of the ridge (Figure 2b) the site errors are practically equal for both ground con-

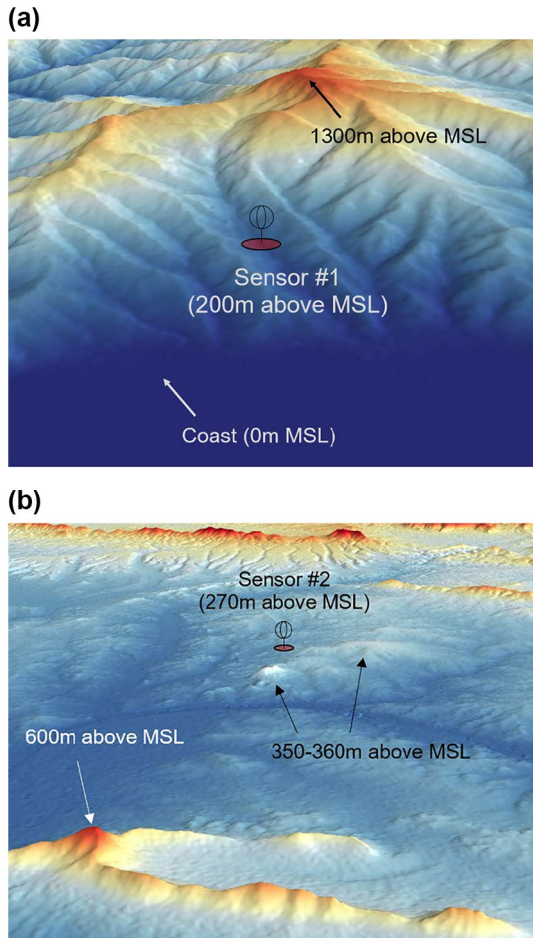


Figure 8. The locations of Sensor #1 and Sensor #2 are plotted using digital elevation model data. (a) Sensor #1 in mountainous terrain close to a coast line. (b) Sensor #2 located at a distance of about 30 km from the 600-m-tall mountain above mean sea level (MSL).

ductivities. A lower ground conductivity ($\sigma = 1$ mS/m) leads to stronger filtering of the high frequency components of the field along the propagation path (see Discussion in Section 4). Thus, the effect of the additional 400 kHz filter is only marginal and does not change the results significantly (see dotted and dash-dotted curves in Figure 6). In conclusion, even for a highly conducting ground for which propagation effects are negligible, a sensor with limited bandwidth will miss recording the field's high-frequency content. This implies that the site errors of the first and subsequent RS are very similar. This point will be further discussed in Section 4.

3.2. Amplitude Site Error

Due to reflection and diffraction processes, amplitude site errors will also occur. Though not discussed as detailed as the angle site errors, a comparison of amplitude site errors caused by different hill elevations (h) for an asymmetric and a symmetric hill in relation to amplitude estimates under flat ground conditions is depicted in Figure 7. The amplitude site error is an even function around $\alpha = 0^\circ$ and $\alpha = 180^\circ$. This is owed to the circumstance that the magnitude $|\vec{H}|$, as the quantity of interest, is a scalar and contains no information on the direction. Therefore, starting at a point of symmetry ($\alpha = 0^\circ$, respectively $\alpha = 180^\circ$, compare Figure 3), both clockwise and counter-clockwise changes in α lead to an equivalent change in the magnitude $|\vec{H}|$. This is in contrast to the angle of the vector \vec{H} , which changes its sign for opposite directions of α and results in an uneven angle site error function around $\alpha = 0^\circ$ and $\alpha = 180^\circ$ (compare Figures 5 and 6). On the top of the ridge, the error can exceed +100% ($h = 500$ m), but also for lower elevations the error can be as high as +50%. At the foot of the ridge, these errors are reduced to values below +20% at azimuths around $\alpha = 0^\circ$ (in front of the ridge and hill), but in the “shadow” of the hill, an attenuation of up to 40% (for $h = 500$ m) prevails. This attenuation is reduced significantly for lower elevations and farther sensor distances, becoming almost negligible at $s = 1.5$ km and $h = 125$ m. These field enhancements and attenuations through close-by mountains have been similarly found in the study presented in Hou et al. (2020). An interesting observation is that even in the back of the symmetric hill, the diffraction

leads to a slight field enhancement of up to +10% (Figure 7b, center), respectively +5% (Figure 7b, bottom) for $h = 500$ m. In contrast to vanishing angle site errors on the top of the symmetric hill, the amplitude error is non-zero, reaching +40% for $h = 500$ m).

3.3. Angle Site Errors of Real Terrain

Sensor supply cables (power and communication) and nearby overhead transmission lines are the most well-known and well-described site error sources in lightning location systems. However, site errors have also been observed for sensors that are not supplied with long cables (for example with photovoltaic power supply directly at the sensor location). For the investigation of potential site errors caused by the local terrain, it was necessary to get data from such sensors. We thus searched specifically for sensor sites with photovoltaic power supply and wireless data communication, where no long cables are deployed. Furthermore, we paid particular attention to make sure that the considered sites do not have in their close proximity any metal fences, railway, or high voltage power transmission lines. As a result of this search, we identified two sensors in existing LLS networks which, despite satisfying the above-mentioned conditions, still exhibit site errors.

Sensor #1 is located close to a coast line with a rapid transition into Alpine terrain, which is depicted in Figure 8. The mountain top visible in the illustration (Figure 8a, red color), is at 1,300 m (above mean sea level)

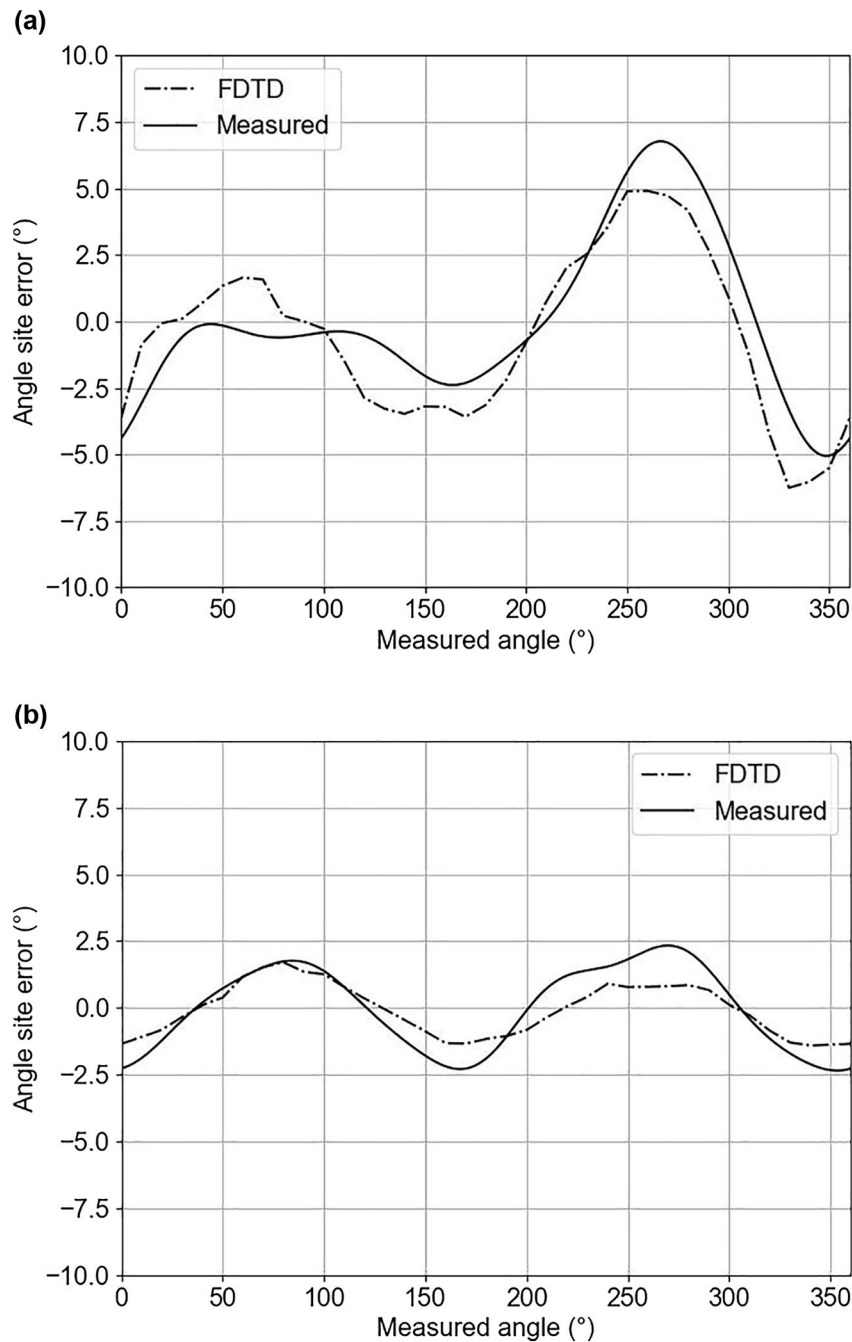


Figure 9. Real measured sensor angle site errors of (a) Sensor #1 and (b) Sensor #2 in comparison with finite-difference time-domain simulation results.

and at a horizontal distance of about 7–8 km from the coast line (sea water has not been considered in the simulations). Aside from the high mountain in close vicinity, it is further characterized by very rough local terrain conditions. Thus, the site error will be expected to be caused by both local reflection and diffraction mechanisms (see Section 2.1) at the same time for any angle of wave incidence along the full azimuth.

We performed 3D-FDTD simulations for these two cases using the exact prevailing geometric terrain conditions and assuming a conductivity of $\sigma = 1$ mS/m. FDTD simulation results for both cases agree well with the measurements (Sensor #1 and #2, see Figure 9). Since a lightning location sensor network as a

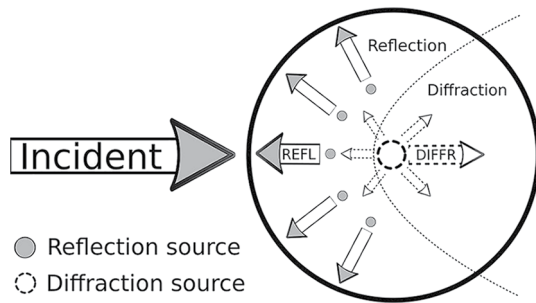


Figure 10. Simplified schematic of an incident field. Reflection and diffraction are depicted with solid and dashed arrows respectively. The solid circle indicates the spatial confinement of a fully symmetric hill. The dotted parabolic line schematically indicates the border between the region where reflection processes and the region where diffraction processes dominantly influence the angle site error (compare with Figure 4).

whole estimates the location of the strike point with high accuracy, this information is used to straight forwardly determine the angle site error of each individual sensor. The curves depicting the measurements in Figure 9 correspond to the average site errors prevailing at the sensors for a large ensemble of events. An interesting observation is that despite the location in very rough terrain, the site errors of Sensor #1 do not exceed a magnitude of 5–7°. This could be explained by a mutual compensation effect of reflection and diffraction mechanisms. It shall be stressed that the site error Θ_{err} depends on and is plotted against the azimuth α , which is the true angle of incidence.

4. Discussion

As already stated in Section 3.1, the site error effect owes to the fact that lightning electromagnetic fields are reflected and diffracted by nearby objects like hills and mountains. This has been discussed in Hou et al. (2020) for a 2-D scenario using cylindrical symmetry FDTD simulation results.

In this work, the results show that spatially confined hills and mountains cause reflection and diffraction components in all directions. A simplified picture of this is shown in Figure 10 which depicts a schematic of these effects for a symmetric hill in a top-down view. The reflection components add field components to the main incident field and rotate the effective H-field at the sensor, while through diffraction new wave fronts are generated from equivalent point sources at the hill, that has a different propagation direction. Depending on the terrain, a mixture of both phenomena will determine the resulting site errors.

The usage of the magnetic field to determine the angle of incidence, as described in Section 2.6, is relevant in terms of angle site errors since short propagation delays between the main incident field and reflected fields (with different propagation directions) might significantly alter the ratio of the magnetic field components H_x and H_y at the field peak. As a consequence, the magnetic direction of the lightning discharge will be estimated incorrectly. Long propagation delays do not impact the results since the angle determination will take place before reflected waves arrive at the sensor.

Figure 11 visualizes this effect in an illustrative manner for the ridge and the symmetric hill (Figure 11 top and bottom) indicating the main incident wavefront (black, solid) and the reflected wavefront (blue, dashed). The propagation delay t_D between the incidence of the main fields at the sensor and the successive arrival of the reflected fields are marked in red. The first reflection components must arrive earlier than the main field peak at t_p , thus $t_D < t_p$, to have a non-zero contribution of the reflected field at the maximum magnitude sampling time instance such that a site error can occur. The case of a high ridge can be considered to highlight the impact of reflection processes on the site error at angles α below 90° (compare Section 3.1, Figure 5a bottom). Close to $\alpha = 0^\circ$ (in the north) the propagation delay t_D is determined by about twice the distance from the sensor to the hillside. The reflected fields (see for example blue dashed curve in Figure 11, middle) arrive too late to cause any effect. Toward 90°, t_D is gradually decreased and the reflected field wavefront starts taking effect. In the case of the symmetric hill, the first significant reflections arriving at the sensor (distance $s = 1.5$ km, Figure 5a bottom) become apparent from $\alpha = 90^\circ$ onwards. The bottom part of Figure 11, illustrates this. At 90° the first reflections are generated when the main wave has already reached the sensor and the reflected waves still need to pass the full distance between the hillside and the sensor. This propagation difference becomes smaller from $\alpha = 90^\circ$ on, resulting in an increased impact on the site error. The maximum impact of the reflection components is observed at about $\alpha = 120^\circ$. This maximum impact on the site error at a relative angle of 120° between the strike point, the reflection sources at the hill, and the sensor location can also be verified visually in Figure 4. There, the outer trails of the site errors, visible further away from the hill center, extent toward $\pm 120^\circ$ relative to the lightning strike point in the west.

As shown in Section 3.1, increased conductivities lead to shorter rise times and as a consequence to a peak value at an earlier time instant and therefore an increased time delay t_D , because the arrival time of the reflections remains unchanged. The site error is therefore shifted toward larger azimuths (for $\alpha < 180^\circ$, re-

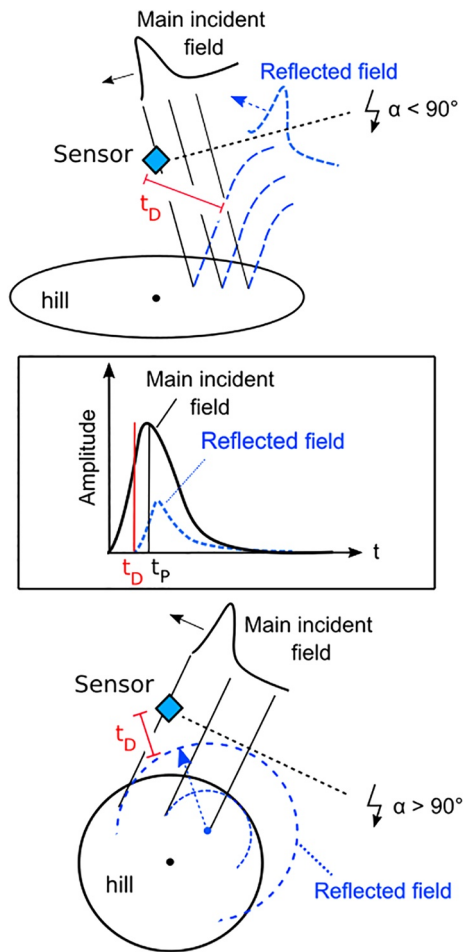


Figure 11. Propagation delay t_b in relation to the different geometric objects and incident field azimuths α . This illustration demonstrates how the incident field angles α are different for symmetric and asymmetric shapes before reflection components can have an impact on the site errors at the moment of the main field peak t_p . In the case of the ridge (top illustration), the reflected waves are produced along an extended surface for angles of incidence smaller than 90° . In contrast, the symmetric hill (bottom illustration), reflects waves from a concentrated area on the surface (indicated by the center of the concentric circles), where the propagation delay t_b becomes significantly small for site errors to occur when the incident angle exceeds 90° .

spectively toward smaller α for the range $\alpha > 180^\circ$) for both scenarios, see Figures 6a and 6b. Finally, a short discussion is in order on the differences between site error behavior between first and subsequent RS. The simulations in this study were performed for a typical subsequent RS with a short rise time (see Soto et al., 2014 or Rachidi et al., 2001). Rise times, however, increase with larger propagation distances over a lossy ground due to stronger attenuation of high frequencies. This is well described in Norton (1941). Despite the relatively close distance to the lightning strike (40 km), we evaluated practically similar site error behavior for first and subsequent RS for both the angle and the amplitude site error. Due to larger rise times and later field peaks of the first RS, shorter propagation delays between the field peak of the main wave and incident reflected waves occur. Therefore, the angle site errors of the first RS start at smaller azimuths α (broadening the site error range) and exhibit even slightly larger angle errors.

5. Conclusion

In this study, the error of the estimated direction of lightning return strokes, called *site error*, due to special geometric terrain conditions in the vicinity of a sensor was evaluated using 3D-FDTD simulations. Such a site error is caused by reflections and diffraction of the electromagnetic fields, due to tall objects, hills, and mountains of different elevations. Reflected and diffracted waves have a different propagation direction and therefore a different orientation compared to the main field component. If these components arrive at the time of the main incident field peak, the ratio between H_x and H_y measured by the sensor is altered in comparison to the ratio above a flat ground, which results in a wrong magnetic direction estimation to the return stroke. This is known as the angle site error. Moreover, changes in the magnitude of the H-field vector will lead to errors in the estimated peak current as well.

After giving an intuitive introduction to the nature of site errors, we investigated the angle and amplitude site errors not only for theoretical objects like ridges (asymmetric hills) or fully symmetric hills of different elevations h but also for real-life terrain. The site errors Θ_{err} on top ridges range between 10° and 20° for elevations between 125 and 500 m. The evaluated amplitude site errors on top of ridges can be as high as +140% for a hill with an elevation of $h = 500$ m, but even for relatively small elevations, more than +30% were observed. At the foot of the simulated hills, the site errors are still significant and can even surpass the site errors registered on the summit due to immediate reflections and

diffraction on the hillsides. It is therefore not recommended to place magnetic direction finding sensors on top or at the foot of hills. However, since the site error declines significantly for larger sensor distances (1.5 km), it should be considered to place sensors at locations where the terrain is flat and sufficiently far away (>1.5 km) from large hills, to avoid significant site errors. The simulations of angle site errors of the real-life scenarios showed good agreement with the sensor site error estimations.

We explained that due to the attenuation of higher frequency components of the field when propagating along a poorly conducting ground, the site error characteristics of subsequent RS and first RS are quite similar. The longer the rise times, the worse the site error behavior, because reflections will arrive at the sensor before the main incident field peak is reached. Even though higher conductivities lead to more obvious differences between the two return stroke types, the differences in the site errors would only be noticeable with sensors of very large bandwidth, but not with a sensor with a bandwidth limited to about 400 kHz.

The findings of this work can contribute to a better understanding of natural site error effects caused by hilly or mountainous terrain in addition to the well-known artificial site error effect caused by cables. The results can be consulted in the future when new sensor sites are selected in the course of LLS network expansion. The proposed technique can also be used for an *a priori* site error rating of LLS sensors.

Data Availability Statement

The illustrations and graphs representing the simulation results of this study are available online (<https://doi.org/10.6084/m9.figshare.14912232>).

Acknowledgments

The authors wish to thank S. Pedebay from Meteorage for providing the angle site errors for two sensor sites without cable connections to the sensor. Further, the authors wish to thank Gerhard Diendorfer for the inspiring and valuable scientific discussions in the course of writing the manuscript.

References

- Arzag, K., Azzouz, Z., Baba, Y., & Ghemri, B. (2019). 3-D FDTD computation of electromagnetic fields associated with lightning strikes to a tower climbed on a trapezoidal mountain. *IEEE Transactions on Electromagnetic Compatibility*, 61(3), 606–616. <https://doi.org/10.1109/TEMC.2019.2895689>
- Baba, Y., & Rakov, V. A. (2016). *Electromagnetic computation methods for lightning surge protection studies*. IEEE Wiley.
- De Dinechin, F., Florent, M., & Istoan, M. (2015). Hardware implementations of fixed-point Atan2. *Paper presented at the 2015 IEEE 22nd Symposium on computer Arithmetic* (pp. 34–41). <https://doi.org/10.1109/ARITH.2015.23>
- Hiscox, W. L., Krider, E. P., Pifer, A. E., & Uman, M. A. (1984). A systematic method for identifying and correcting "site errors" in a network of magnetic direction finders. *Paper presented at the International Conference on lightning and Static Electricity*. (ICOLSE).
- Hou, W., Azadifar, M., Rubinstein, M., Rachidi, F., & Zhang, Q. (2020). On the propagation of lightning-radiated electromagnetic fields across a mountain. *IEEE Transactions on Electromagnetic Compatibility*, 62, 1–2147. <https://doi.org/10.1109/TEMC.2019.2947095>
- Kohlmann, H. (2020). *FDTD simulation of lightning electromagnetic fields - an approach with the software package MEEP*. TU Wien. Retrieved from <http://hdl.handle.net/20.500.12708/1235>
- Kohlmann, H., & Schulz, W. (2021). Comparison of 3-D and 2-D cylindrical symmetry FDTD simulation results of a lightning strike to Gaisberg with ALDIS sensor measurements. *IEEE Transactions on Electromagnetic Compatibility*, 9, 1–9. <https://doi.org/10.1109/TEMC.2021.3073787>
- Li, D., Azadifar, M., Rachidi, F., Rubinstein, M., Diendorfer, G., Sheshyekani, K., et al. (2016). Analysis of lightning electromagnetic field propagation in mountainous terrain and its effects on ToA-based lightning location systems. *Journal of Geophysical Research: Atmospheres*, 121(2), 895–911. <https://doi.org/10.1002/2015JD024234>
- Li, D., Azadifar, M., Rachidi, F., Rubinstein, M., Paolone, M., Pavanello, D., et al. (2016). On lightning electromagnetic field propagation along an irregular terrain. *IEEE Transactions on Electromagnetic Compatibility*, 58, 161–171. <https://doi.org/10.1109/TEMC.2015.2483018>
- Li, D., Luque, A., Rachidi, F., Rubinstein, M., Azadifar, M., Diendorfer, G., & Pichler, H. (2019). The propagation effects of lightning electromagnetic fields over mountainous terrain in the earth-ionosphere waveguide. *Journal of Geophysical Research: Atmospheres*, 124(24), 14198–14219. <https://doi.org/10.1029/2018JD030014>
- Li, D., Rubinstein, M., Rachidi, F., Diendorfer, G., & Schulz, W. (2018). Analysis of location accuracy of ToA-based lightning location systems in mountainous terrain. *Paper presented at the International Conference on Atmospheric Electricity*. <https://doi.org/10.1002/2017JD027520>
- Li, D., Rubinstein, M., Rachidi, F., Diendorfer, G., Schulz, W., & Lu, G. (2017). Location accuracy evaluation of ToA-based lightning location systems over mountainous terrain. *Journal of Geophysical Research: Atmospheres*, 122(21), 11,760–11,11. <https://doi.org/10.1002/2017JD027520>
- Li, D., Zhang, Q., Wang, Z., & Liu, T. (2014). Computation of lightning horizontal field over the two-dimensional rough ground by using the three-dimensional FDTD. *IEEE Transactions On Electromagnetic Compatibility*, 56(1), 143–148. <https://doi.org/10.1109/TEMC.2013.2266479>
- MEEP Documentation. (2021). Retrieved from <https://meep.readthedocs.io>
- MEEP Github Repository. (2021). Retrieved from <https://github.com/NanoComp/meep>
- Norton, K. A. (1941). The calculation of ground-wave field intensity over a finitely conducting spherical earth. *Proceedings of the IRE*, 29(12), 623–639. <https://doi.org/10.1109/JRPROC.1941.233636>
- Nucci, C. A., Mazzetti, G., Rachidi, F., & Ianoz, M. V. (1988). On lightning return stroke models for "LEMP" calculations. *Presented at the 1988 19th International Conference on lightning Protection (ICLP)*.
- Oskooi, A. F., Roundy, D., Ibanescu, M., Bermel, P., Joannopoulos, J. D., & Johnson, S. G. (2010). Meep: A flexible free-software package for electromagnetic simulations by the FDTD method. *Computer Physics Communications*, 181(3), 687–702. <https://doi.org/10.1016/j.cpc.2009.11.008>
- Rachidi, F., Janischewskyj, W., Hussein, A. M., Nucci, C. A., Guerrieri, S., Kordi, B., & Chang, J.-S. (2001). Current and electromagnetic field associated with lightning-return strokes to tall towers. *IEEE Transactions on Electromagnetic Compatibility*, 43(3), 356–367. <https://doi.org/10.1109/15.942607>
- Schulz, W. (1997). *Performance Evaluation of lightning location systems (PhD Thesis)*. Technical University of Vienna.
- Schulz, W., & Diendorfer, G. (2002). Amplitude site error of magnetic direction finder. *Paper presented at the 2002 26th International Conference on lightning Protection* (pp. 4–7).
- Schulz, W., Diendorfer, G., Hofbauer, F., Stimmer, A., & Mair, M. (1998). Site errors in magnetic direction finding due to buried cables. *Paper presented at the 1998 24th International Conference on lightning Protection (ICLP)*.
- Soto, E., Perez, E., & Herrera-Murcia, J. G. (2014). Electromagnetic field due to lightning striking on top of a cone-shaped mountain using the FDTD. *IEEE Transactions on Electromagnetic Compatibility*, 56(5), 1112–1120. <https://doi.org/10.1109/TEMC.2014.2301138>
- Suzuki, Y., Araki, S., Baba, Y., Tsuboi, T., Okabe, S., & Rakov, V. A. (2016). An FDTD study of errors in magnetic direction finding of lightning due to the presence of conducting structure near the field measuring station. *Atmosphere*, 7(7), 92. <https://doi.org/10.3390/atmos7070092>
- Taflove, A., & Hagness, S. C. (2005). *Computational electrodynamics: The finite-difference time-domain method* (3rd ed.). Artech house.

- Yee, K. (1966). Numerical solution of initial boundary value problems involving Maxwell's equations in isotropic media. *IEEE Transactions on Antennas and Propagation*, 14(3), 302–307. <https://doi.org/10.1109/tap.1966.1138693>
- Zhang, J., Zhang, Q., Zhou, F., Ma, Y., Pan, H., & Hou, W. (2019). Computation of lightning-induced voltages for striking oblique cone-shaped mountain by 3-D FDTD Method. *IEEE Transactions on Electromagnetic Compatibility*, 61(5), 1543–1551. <https://doi.org/10.1109/TEMC.2018.2869607>